J Geod
DOI 10.1007/s00190-015-0801-9

ORIGINAL ARTICLE

Network-based estimation of time-dependent noise in GPS position time series

Ksenia Dmitrieva · Paul Segall · Charles DeMets

Received: 26 July 2014 / Accepted: 1 March 2015

Abstract Some estimates of GPS velocity uncertainties are very low, <0.1 mm/year with 10 years of data. Yet, residual velocities relative to rigid plate models in nominally stable plate interiors can be an order of magnitude larger. This discrepancy could be caused by underestimating low-frequency time-dependent noise in position time series, such as random walk. We show that traditional estimators, based on individual time series, are insensitive to low-amplitude random walk, yet such noise significantly increases GPS velocity uncertainties. Here, we develop a method for determining representative noise parameters in GPS position time series, by analyzing an entire network simultaneously, which we refer to as the network noise estimator (NNE). We analyze data from the aseismic central-eastern USA, assuming that residual motions relative to North America, corrected for glacial isostatic adjustment (GIA), represent noise. The position time series are decomposed into signal (plate rotation and GIA) and noise components. NNE simultaneously processes multiple stations with a Kalman filter and solves for average noise components for the network by maximum likelihood estimation. Synthetic tests show that NNE correctly estimates even low-level random walk, thus providing better estimates of velocity uncertainties than conventional, single station methods. To test NNE on actual data, we analyze a heterogeneous 15 station GPS network from the central-eastern USA, assuming the noise is a sum of random walk, flicker and white noise. For the horizontal time series, NNE finds higher average random walk than the standard individual station-based method, leading to velocity uncertainties a factor of 2 higher than traditional methods.

Keywords GPS noise · Velocity uncertainty · Power-law noise · Error analysis

1 Introduction

GPS station velocities are widely used for studying various geophysical phenomena (Segall and Davis 1997), including plate movement (Thatcher 2003), strain accumulation (Bennett et al. 2003; Serpelloni et al. 2005), volcanic deformation (Puskas et al. 2007; Bonforte and Puglisi 2006), post-glacial rebound (Lidberg et al. 2007; King et al. 2010), subsidence (Lü et al. 2008; Psimoulis et al. 2007), and sea-level change (Wöppelmann et al. 2007; Teferle et al. 2006). Permanent high-precision GPS networks are becoming more common, and today it is possible to find time series spanning over 20 years. However, to fully utilize the GPS data it is necessary to know the uncertainties in the station velocities. For example, in intraplate regions, such as the New Madrid Seismic Zone in the central USA, there is controversy as to the significance of measured GPS velocities (Calais et al. 2006; Calais and Stein 2009; Frankel et al. 2012). More generally, the interpretation of the data depends crucially on the estimated measurement noise level. Additionally, signal-to-noise level is crucial in determining the appropriate level of regularization in geodetic inversions (Kusche and Schrama 2005; Pritchard et al. 2002). It is also important to estimate the velocity uncertainties correctly when combining GPS data with independent geodetic or geologic data (Liu et al. 2000; Papanikolaou et al. 2005; Hill et al. 2010).

K. Dmitrieva (✉) · P. Segall
Stanford University, Stanford, CA 94305, USA
e-mail: dmitrieva@stanford.edu

C. DeMets
University of Wisconsin, Madison, WI 53706, USA

Published online: 24 March 2015

GPS velocity uncertainties are determined by the noise level in the position data and the length of the time series. Noise in GPS time series is generally considered to be composed of noise uncorrelated in time ("white") and noise that is temporally correlated (Mao et al. 1999). While white noise affects the uncertainty in velocity, this can be significantly reduced through repeated measurements. In contrast, time-dependent noise becomes more influential with increasing length of the time series and generally dominates the error in velocity estimates. If not properly accounted for, long period noise could lead to misleadingly small velocity uncertainties (Langbein 2012).

Time-dependent noise is commonly characterized by power-law models, where the spectral amplitude is assumed to vary as $F(f) \propto f^{-n}$, where f is frequency and n is the power-law index (Agnew 1992). Time-dependent GPS noise can be represented as a linear combination of flicker noise ($n = 1$) and random walk ($n = 2$) or with a non-integer power-law index (e.g., Zhang et al. 1997; Mao et al. 1999). For the same amplitude, the higher the power-law index, the more it increases the velocity uncertainty. Even low levels of random walk can significantly increase the velocity uncertainty (Williams 2003a). The sources of time-dependent noise are not completely understood. Some research has shown that monument instability leads to random walk behavior (Wyatt 1989). The origin of flicker noise is less clear, but time-variable satellite geometry, long-term orbit mismodeling, and multipath have been suggested as possible contributors (King and Watson 2010; Ray et al. 2008; Jiang et al. 2014).

Time-dependent noise can be roughly estimated from a power spectrum of the GPS time series (Langbein and Johnson 1997; Zhang et al. 1997; Santamaría-Gómez et al. 2011). However, this spectral fitting is not precise. The more commonly used method is maximum likelihood estimation (MLE) applied to individual component time series (e.g., Langbein 2004, Williams et al. 2004).

In many, but not all, studies a linear trend is estimated and the residuals about that trend are modeled as a sum of noise processes. In doing so, the trend is assumed to be true signal. It is also possible to determine the signal a priori based on a physical model, and associate the residuals with a sum of noise processes. In this paper, we refer to MLE estimates on individual time series with linear trends either estimated or pre-subtracted as standard MLE (sMLE). In sMLE, each time series is individually processed by finding noise parameters that fit the data with the highest likelihood. Different groups have estimated either a single non-integer power-law index or a combination of random-walk and flicker noise. Langbein (2012) showed that assuming a single power-law representation, when the underlining model is a combination of flicker noise and random walk, it can lead to underestimation of velocity uncertainty by a factor of two. Other methods include least squares variance component estimation (Amiri-Simkooei et al. 2007) and applying the Allan variance of the rate to the time series (Hackl et al. 2011).

Most studies suggest that the best representation of time-dependent GPS noise is flicker noise with no or very little random walk (Williams et al. 2004; Hackl et al. 2011; Zhang et al. 1997; Amiri-Simkooei et al. 2007). However, random walk is difficult to accurately determine with a short time series or if the variance of flicker noise is large, thus masking the random walk (Langbein 2012). Hence, it is possible that random walk is present in the data, but not easily detectable. This could be a cause for concern since the presence of low-frequency noise in the data (e.g., random walk) can significantly affect velocity uncertainty (Williams 2003a; Langbein 2012). For example, a velocity from 10 years of daily position data with just white noise with a standard deviation of 1 mm would have an uncertainty of 0.006 mm/year. With an additional 4 mm/year$^{0.25}$ flicker noise, the uncertainty increases to 0.13 mm/year, and with added random walk with amplitude of 1.5 mm/year$^{0.5}$ the uncertainty becomes 0.5 mm/year.

There are perhaps two approaches to accounting for noise in modeling GPS time series. One approach would be to determine the noise characteristics of each station in a network individually, and then weight the different stations accordingly (some accounting for spatial correlation between stations would also be required). This approach is sensible in that we expect different stations to have variable monument stability and multipath characteristics. An alternate approach would be to determine representative noise parameters for classes of stations, grouped based on monumentation type or other characteristics. This approach is already used by many geophysical modeling studies that employ representative noise parameters gleaned from the literature and is the approach we take in this study.

Here, we introduce a network noise estimator (NNE) which processes a network of stations simultaneously, using a Kalman filter to iteratively compute the likelihood, and solves for a set of average noise parameters for the network by maximizing the likelihood. The underlying assumption in our approach is that tectonic signals must be spatially coherent, whereas at least some noise sources are spatially incoherent. From a crustal deformation viewpoint, two stations with separation smaller than the characteristic lengths of tectonic processes should see similar signals. Any incoherent motion, such as caused by local processes (e.g., local landsliding or subsidence), is considered noise from a tectonic perspective.

Some GPS noise processes, such as monument instability and multipath, are spatially incoherent, whereas others, such as orbit errors and uncompensated tropospheric delays, will be spatially correlated. Here, for simplicity in this initial study, we assume all noise to be spatially incoherent, although this will be modified in future implementations.

Because our goal is to characterize average GPS noise parameters, it is advantageous to focus on areas where the signal is well understood. Therefore, we analyze data from stable plate interiors where the signal is dominated by plate rotation, possibly with effects of glacial isostatic adjustment (GIA). The key idea behind this approach is that the signal is assumed to be well characterized, while the noise is unknown.

NNE has some advantages over sMLE. First, our method analyzes multiple stations simultaneously, rather than individual time series as in sMLE. In doing so we forgo the ability to estimate noise parameters at every station, in favor of estimating more robust noise parameters for the ensemble.

We show below that a network estimate is not the same as the average of individual sMLE estimates. The fact that NNE estimates a single set of noise parameters for groups of stations could be viewed as a disadvantage of the approach; however, we believe that this is compensated by the ability to obtain more robust estimates of long period noise. Secondly, with sMLE it is common to remove or estimate best-fitting trends in the time series. In contrast, we only remove trends due to known processes, such as plate rotation and GIA. Some time-dependent noise can produce apparent trends in time series. If such a trend is removed, it could potentially bias noise estimation, possibly leading to an underestimation of velocity uncertainty.

Of course, it is possible to take the same approach with sMLE and only remove trends due to known processes. Thirdly, the Kalman filter approach allows one to update estimates with new data without having to reprocess all of the older data.

Our goal in this paper is to demonstrate a new method that determines representative levels of noise in the GPS position time series. We first describe the method and then demonstrate its capability of working on synthetic and actual GPS data. We show that the NNE can resolve weak random walk in the presence of flicker noise that is not revealed by sMLE, demonstrating the effectiveness of the method.

2 Network noise estimator (NNE) description

We represent the noise as a combination of random walk, flicker, and white noise. We choose this combination as the different noise components could represent different physical noise processes. Additionally, Langbein (2012) showed that using a sum of power law and white noise may result in a significant underestimation of low-frequency noise.

We describe the GPS time series as a combination of signal, which is spatially coherent, and noise. Since we restrict attention to stable plate interiors, the signal is composed of plate rotation and possible GIA displacements. The station coordinate time series is described as

$$X(t) = X(t_0) + (t - t_0)(\mathbf{M} \cdot \Omega + V_{\mathrm{GIA}}) + L(\tau^2) + \mathrm{FL}(\rho^2) + \varepsilon. \quad (1)$$

Here, X is station position, t is time, t_0 is initial time (i.e., the beginning of the time series), $\mathbf{M}$ is a matrix of geocentric station positions that maps the pole of rotation to velocity, Ω is the Euler pole, V_{GIA} is the velocity due to GIA, $L(\tau^2)$ is random walk at t (with variance τ^2), $\mathrm{FL}(\rho^2)$ is flicker noise at t (with variance ρ^2), $\varepsilon \sim \mathcal{N}(0, \mathbf{R})$ is observational white noise, $\mathbf{R} = \sigma^2\Sigma$, where σ is white noise variance, and Σ is the normalized data covariance matrix from GPS processing including off-diagonal terms. In case of uncorrelated measurements (e.g., for networks processed with PPP), Σ becomes a diagonal matrix.

Note that the plate rotation and GIA signals could be subtracted from the data prior to estimation. For simplicity in the description of the method, we omit the GIA signal. However we will keep the plate rotation component to illustrate how a well-characterized signal can be included in the NNE.

Our algorithm is based on the Kalman filter, in which Eq. (1) is written in the form of a state-space model. All of the components in (1), with the exception of flicker noise, are easily represented in a state-space model. Davis et al. (2005) showed that flicker noise can be approximated over a finite bandwidth as a linear combination of independent first-order Gauss–Markov (FOGM) processes, yielding what we refer to as finite bandwidth flicker noise (FBFN). Flicker noise has power spectral density

$$P(f) = \frac{\rho^2}{\pi f_s^{1/2}} \frac{1}{f}, \quad (2)$$

where f is frequency, f_s is the sampling frequency, and ρ is the square root of the variance of the flicker noise with units mm/year$^{0.25}$ (e.g., Langbein 2004).

An FOGM process has a spectral density function

$$P(f) = \frac{\beta^2}{\bar{f}^2 + 4\pi^2 f^2}. \quad (3)$$

The FOGM spectrum is flat at long periods, but decays as $1/f^2$ above the corner frequency $\bar{f}$. With FBFN the sum of shifted FOGM processes approximates a f^{-1} spectrum as a combination of f^0 and f^{-2} segments. Davis et al. (2005) recommend a sum of GM processes such that the periods at the corner frequencies, $1/\bar{f}_j$ of successive FOGM processes, are chosen to increase geometrically with a spacing ratio s, so that $\bar{f}_{j+1} = \bar{f}_j/s$, and the spectral densities β_j^2 are chosen such that $\beta_j^2/2\bar{f}_j$ are equal (Fig. 1). From a practical standpoint, we only need the FBFN to approximate f^{-1} for frequencies where flicker noise influences the total noise spectrum. We discuss an appropriate choice of corner frequencies of FBFN later in this article.

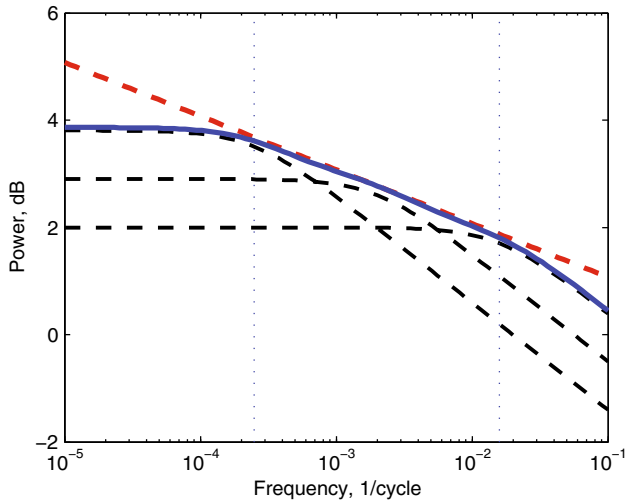

Fig. 1 Representation of flicker noise as a sum of Gauss–Markov components. Power spectrum of independent Gauss–Markov components offset in amplitude and frequency (*black dashed lines*). Sum of the Gauss–Markov components (*solid blue line*). Power spectrum of flicker noise $(1/f)$ (*dashed red line*). *Blue vertical lines* mark the corner frequencies of the first and the last Gauss–Markov components

The relationship between the flicker noise variance ρ^2 and spectral density β^2 can be derived from Eqs. 2 and 3:

$$\rho^2 = \sum_{j=1}^{m} \frac{\beta_j^2 \pi f_s^{1/2} f_m}{\left(\bar{f}_j^2 + 4\pi^2 f_m\right)}, \tag{4}$$

where m is the number of FOGM components and f_m is a geometrical midpoint between the highest and the lowest corner frequencies.

Let Z^m be the vector of Gauss–Markov process at t. Each FOGM process is defined by its spectral density β_j^2 and corner frequency $\bar{f}_j$. However, we write Z^m as functions of flicker noise variance ρ^2, as our goal is to estimate this parameter. Now, dropping the GIA component, Eq. (1) becomes

$$X(t) = X(t_0) + (t - t_0)(\mathbf{M} \cdot \Omega) + L(\tau^2) + Z^1(\rho^2) + Z^2(\rho^2) + \cdots + Z^m(\rho^2) + \varepsilon. \tag{5}$$

The Kalman filter recursively evaluates the state of a dynamical system based on the measurements and an underlying model. The state at each time step k is represented by the state vector x_k. For the model described above, we write the state vector as

$$\mathbf{x}_k = [\Omega_1, \Omega_2, \Omega_3, L_1, L_2, \ldots, L_n, Z_1^1, \ldots, Z_1^m, \ldots, Z_n^1, \ldots, Z_n^m]^T, \tag{6}$$

where L_i is the random walk of the ith time series, Z_i^j is the jth Gauss–Markov component of the ith time series, and n is the number of time series. Note that each FOGM process is represented individually as a component of the state vector.

The length of the state vector is $3 + n + nm$: three terms for the rotation pole, a term for random walk for each time series, and m terms for each time series representing flicker noise as a sum of FOGM processes.

The observation equation can be written in general form as:

$$\mathbf{d}_k = \mathbf{H}_k \mathbf{x}_k + \varepsilon, \tag{7}$$

where k indexes an epoch or time step, $\mathbf{d}$ is the vector of data, $\mathbf{H}$ is a measurement matrix, and $\varepsilon \sim \mathcal{N}(0, \mathbf{R})$ is the vector of observation errors. In our case, the observation equation implements Eq. (5), where $\mathbf{H}$ is a $n \times (3 + n + nm)$ matrix given by

$$\mathbf{H} = \left[(t - t_0)\mathbf{M}, \mathbf{I}_{n \times n(1+m)}\right], \tag{8}$$

where $\mathbf{I}$ denotes a block matrix of identity matrices (for the random walk and flicker noise components). Assuming the measurement errors are equal and uncorrelated between station components, the observation noise covariance matrix is $\mathbf{R} = \sigma^2\mathbf{I}$.

The equation relating state vectors $\mathbf{x}$ at times t_k, and t_{k+1} is the state transition equation:

$$\mathbf{x}_{k+1} = \mathbf{F}_{k+1}\mathbf{x}_k + \eta_{k+1}, \tag{9}$$

where $\mathbf{F}$ is a state transition matrix that maps state at k to state $k + 1$, and $\eta \sim \mathcal{N}(0, \mathbf{Q}_{k+1})$ is a vector of process noise with covariance matrix $\mathbf{Q}$.

To create the state-space model, we need to construct the matrices $\mathbf{F}$, $\mathbf{H}$, $\mathbf{Q}$, and $\mathbf{R}$ ($\mathbf{H}$ and $\mathbf{R}$ previously defined). The state transition matrix $\mathbf{F}$ is a block diagonal matrix with each block corresponding to each part of the state vector, which in our case includes the pole of rotation, random walk, and flicker noise. For both the rotation pole and random walk, the blocks in $\mathbf{F}$ are identity matrices. The state transition matrix can thus be written as

$$\mathbf{F}_k = \begin{bmatrix} \mathbf{I}_{3\times3} & \mathbf{0} & \mathbf{0} \\ \mathbf{0} & \mathbf{I}_{n\times n} & \mathbf{0} \\ \mathbf{0} & \mathbf{0} & \mathbf{F}^{\mathrm{FN}}_{k,nm\times nm} \end{bmatrix}, \tag{10}$$

where $\mathbf{I}_{3\times3}$ and $\mathbf{I}_{n\times n}$ are identity matrices for the pole of rotation and random walk, respectively, and $\mathbf{F}^{\mathrm{FN}}_{k,nm\times nm}$ is a state transition matrix for all Gauss–Markov components for each station.

The process noise covariance matrix is constructed as follows:

$$\mathbf{Q}_k = \begin{bmatrix} \mathbf{0_{3\times3}} & \mathbf{0} & \mathbf{0} \\ \mathbf{0} & \tau^2\delta t_k & \mathbf{0} \\ \mathbf{0} & \mathbf{0} & \mathbf{Q}^{\mathrm{FN}}_k \end{bmatrix}, \tag{11}$$

where $\delta t_k = (t_k - t_{k-1})$ is the time step. The first block $\mathbf{0_{3\times3}}$ corresponds to the pole of rotation (constant in time) and the two other blocks correspond to random walk $(n \times n)$ and flicker noise $(nm \times nm)$, respectively. Here, we have

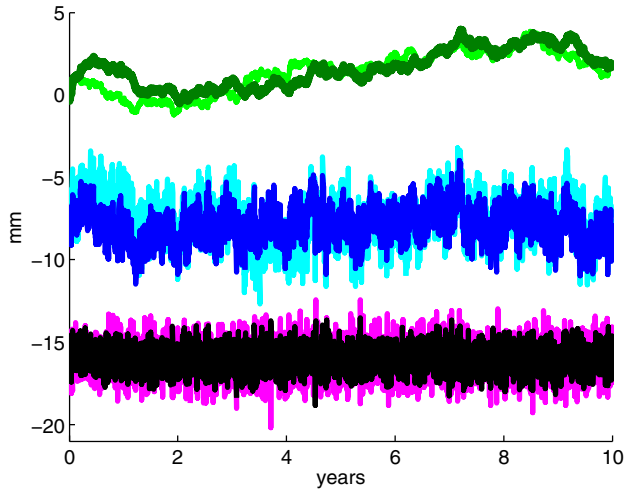

Fig. 2 An example of simulated noise components input and estimated by the Kalman filter. *Light green*, *cyan*, and *magenta* indicate input random walk noise, flicker noise, and white noise, respectively. *Dark green*, *blue*, and *black* indicate the corresponding Kalman filter estimates of these noise components. Input noise: 1 mm/year$^{0.5}$ of random walk, 4 mm/year$^{0.25}$ of flicker noise, and 1 mm of white noise, fixed to correct values during filtering. Arbitrary offsets for clarity

taken account of the fact that for random walk $\mathbf{F_k} = \mathbf{I}$ and $\mathbf{Q_k} = \tau^2 \delta \mathbf{t_k}$ (e.g., Segall and Matthews 1997).

Davis et al. (2005) gives the state transition matrix $\mathbf{F}^{\mathrm{FN}}$ and process noise covariance matrix $\mathbf{Q}^{\mathrm{FN}}$ to implement the approximation of flicker noise. (These matrices are found in the Appendix of this paper.)

The Kalman filter recursively solves Eqs. (7) and (9) through a series of prediction and update steps. During the prediction step, state and state covariance are predicted based on the underlying stochastic model. Then the predicted data are compared to the actual data and the state is updated depending on the relative accuracy of the observation and the prediction. (The Kalman filter equations are found in the Appendix.)

To illustrate how the Kalman filter distinguishes the different noise components in the data, we generate 20 different time series each spanning 10 years with daily sampling. Synthetic time series are constructed with random walk noise (1 mm/year$^{0.5}$), flicker noise (4 mm/year$^{0.25}$) and white noise (1 mm). The Kalman filter decomposes the time series into different constituents. The noise components estimated by the Kalman filter are reasonably consistent with the input noise, as shown by an example in Fig. 2.

We seek the maximum likelihood estimate of the noise parameters (τ, ρ, σ). NNE recursively computes the likelihood within the Kalman filter for a given set of (τ, ρ, σ), as described below. A constrained optimization routine is then used to find the parameter set that maximizes the likelihood.

Define a vector of unknowns $\Theta = [\tau^2, \rho^2]^{\mathbf{T}}$. It was shown (Tremayne and Harvey 1983; Segall and Matthews 1997) that the likelihood can be expressed as:

$$\mathcal{L}(\Theta/\sigma^2|\mathbf{d}) = -0.5(N_d - N_d \log N_d) - 0.5 \sum_{k=1}^{N} \log |\mathbf{V}_k| - 0.5 N_d \log \left[\sum_{k=1}^{N} \mathbf{v}_k^T \mathbf{V}_k^{-1} \mathbf{v}_k \right], \quad (12)$$

where N_d is the total number of data, N is the number of epochs, $\mathbf{v}_k = \mathbf{d}_k - \mathbf{H}_k x_{k|k-1}$ is the kth innovation, $\mathbf{V}_k = \mathbf{R}_k + \mathbf{H}_k \Sigma_{k|k-1} \mathbf{H}_k^T$ is the covariance matrix of the kth innovation, $x_{k|k-1}$ is a conditional mean, and $\Sigma_{k|k-1}$ is the state covariance. The notation $_{i|j}$ denotes the mean or covariance at epoch i given data through epoch j. The MLE estimate of σ^2 is

$$\hat{\sigma}^2 = \sum_{k=1}^{N} \frac{1}{N_d} \mathbf{v}_k^T \mathbf{V}_k^{-1} \mathbf{v}_k. \quad (13)$$

The optimization routine returns the value $\hat{\mathbf{\Theta}}/\sigma^2$ that maximizes $\mathcal{L}(\Theta/\sigma^2|\mathbf{d})$ in (12), and given $\hat{\sigma}^2$ from (13) we determine the MLE estimates $\hat{\tau}^2$, $\hat{\rho}^2$.

While there are certain advantages to employing a Kalman filter, it should be noted that for every state-space model there is an equivalent "batch" estimator that treats all time series in one estimate. Thus, it is possible to estimate a network-wide MLE estimate without using a Kalman filter.

3 Tests of the method

3.1 Tests of FBFN

FBFN is characterized by four parameters: flicker noise variance (ρ^2), the highest and the lowest corner frequencies ($\bar{f}_1$ and $\bar{f}_m$), and spacing ratio s. ρ^2 is the variance of the flicker noise we aim to approximate. Our goal is to approximate flicker noise within a certain frequency band. One reasonable way to choose the corner frequencies is to consider the crossover frequencies between white and flicker noise for the highest corner frequency and between flicker noise and random walk for the lowest frequency. However, Langbein (2012) showed that random walk can contribute to the velocity uncertainty at frequencies higher than flicker noise–random walk crossover. Additionally, Fig. 1 shows that the rollover in an FOGM process is gradual, meaning that the FBFN close to the first and last corner frequencies will not represent flicker noise properly. For these reasons, we are conservative in choosing the corner frequencies. We set the lowest frequency at a period longer than the duration of the time series, and the highest corner frequency at half the sampling rate or 0.5/day (the Nyquist frequency).

The spacing ratio determines how many FOGM processes are used in the FBFN approximation. Increasing the number of FOGM processes makes the FBFN spectrum closer to true flicker noise, but results in a heavier computational burden.

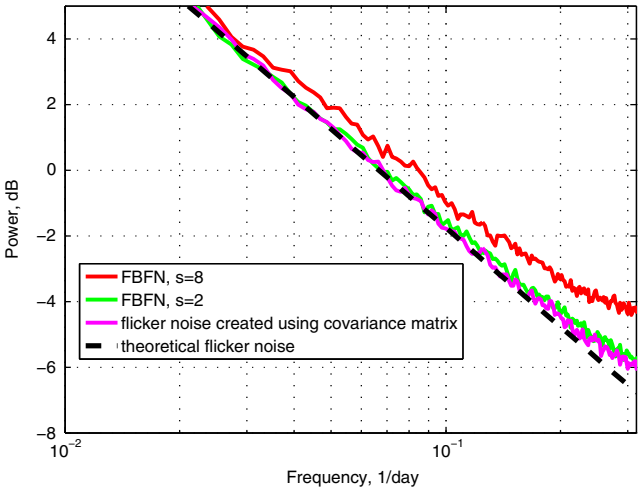

Fig. 3 High-frequency part of the averaged power spectrum of 100 FBFN components with spacing ratio of 8 (*red*) and 2 (*green*) and 100 averaged flicker noise components created using covariance matrix (*magenta*). The *black dashed line* indicates the theoretical power spectrum of flicker noise

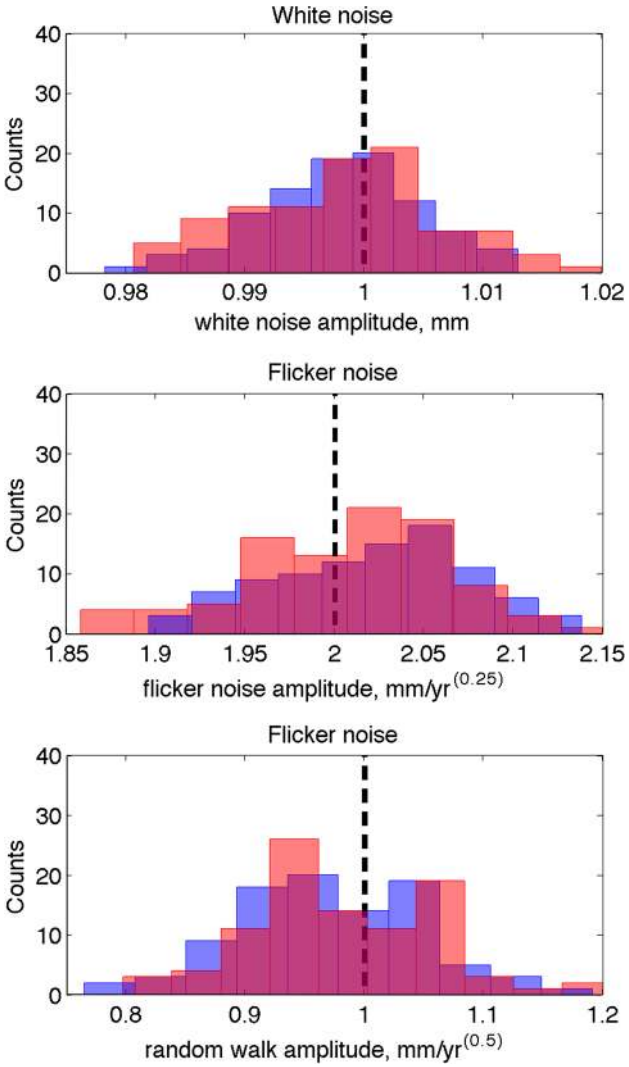

Fig. 4 Distributions of estimated noise amplitudes after running NNE on synthetically generated data (100 trials). The *vertical black dashed lines* indicate the true values of the noise parameters. *Blue histograms* correspond to flicker noise created using a covariance matrix approach, and *red histograms* correspond to flicker noise created as FBFN

Davis et al. (2005) recommend using a multiple of 2 as the spacing ratio. Figure 3 shows the high-frequency part of the power spectrum for FBFN generated with spacing ratios of 8 and 2 as well as the flicker noise generated using the covariance matrix approach (Langbein 2004). Since a spacing ratio of 2 provides the closest approximation to theoretical flicker noise, we choose to use this value. Note that at very high frequencies (>0.21/day), all realizations of flicker noise "flatten". This happens due to aliasing (Kirchner 2005); noise at frequencies higher than the sampling frequency (1/day) is aliased into the power spectrum. This effect could bias estimates of white noise, but it appears to be a small effect for $s = 2$ and we save further quantification of this effect for future investigation. In this work, we take $s = 2$ and set the highest corner frequency to be half the sampling rate, or 0.5/day. With 16 FOGM components, this yields an FBFN model that spans periods of 2 days to much longer than 20 years (e.g., longer than the data series).

To examine how accurately FBFN approximates flicker noise within the NNE, we test it on synthetic data. We generate a network of eight time series with 10 years of daily positions, consisting of random walk, flicker noise and white noise, and then estimate the noise parameters. We repeat this 100 times for the same noise parameters, but different realizations. This is done twice: first, we generate flicker noise as FBFN, in accordance with our state-space model. Secondly, we generate flicker noise with the covariance matrix approach (Langbein 2004). Figure 4 shows histograms of the estimated parameters for both representations of flicker noise, as well as the true value of each parameter. The histograms show no significant difference between the two methods of generating flicker noise. This supports the use of FBFN in the state space model.

3.2 Comparison of NNE and sMLE using synthetically generated data

In this section, we test the performance of both NNE and sMLE (e.g., Langbein 2004) in estimating noise variances on synthetic data. We implement sMLE employing a Cholesky factorization of the covariance matrix for computational efficiency. Maximization of the likelihood is performed by a built-in `MATLAB` constrained optimization routine.

We generate seven synthetic networks with 10 years of data at ten stations (20 horizontal time series). Each time

series is a sum of random walk, flicker noise, and white noise. Since there is no plate rotation, only spatially uncorrelated noise, the geometry of the network is not important. To test the method's performance at different ratios of random walk to flicker noise variance, we keep white and flicker noise the same for all seven networks ($\sigma = 1$ mm, $\rho = 4$ mm/year$^{0.25}$), but vary random walk from 0.1 to 1.5 mm/year$^{0.5}$ for each test. Synthetic flicker noise is generated using the power-law covariance matrix.

We show theoretical as well as empirical power spectra of three of the seven synthetic networks in Fig. 5. When random walk is the smallest ($\tau = 0.1$ mm/year$^{0.5}$), it barely contributes to the total noise. Moderate random walk ($\tau = 0.8$ mm/year$^{0.5}$) dominates the spectra only at very low frequencies. Strong random walk ($\tau = 1.5$ mm/year$^{0.5}$) dominates the time series at periods longer than ~2 years.

The results of NNE and sMLE estimates are shown in Fig. 6. Since sMLE estimates random walk, flicker, and white noise for every time series, while NNE provides a single set of average parameters for the whole network, we compare network estimates with median and quartile sMLE estimates. Both methods estimate white noise and flicker noise well for all seven values of random walk variance. However, NNE outperforms sMLE in estimating the random walk variance. The lower the random walk, the more does sMLE underestimate its value. For example, for a random walk variance of $\tau = 0.5$ mm/year$^{0.5}$, sMLE estimates zero random walk variance in 75 % of the cases, whereas the NNE estimate is remarkably similar to the true value. Even for larger values of random walk, sMLE underestimates random walk, while NNE estimates more accurate values of τ. sMLE estimates become more accurate when random walk increases in amplitude. We conclude that sMLE may not detect low-level random walk even when it is present in the data.

We calculate velocity uncertainty from the noise estimates. For all the cases when sMLE underestimated random walk, the estimated velocity uncertainty is also underestimated (Fig. 6). For example, for random walk $\tau = 0.5$ mm/year$^{0.5}$, the median sMLE velocity uncertainty is 0.13 mm/year, while the true value is 0.21 mm/year, which is 1.8 times higher. For $\tau = 1$ mm/year$^{0.5}$ the median sMLE velocity uncertainty is 0.19 mm/year, while the true value is 0.35 mm/year. Once random walk is large, 1.5 mm/year$^{0.5}$, the discrepancy between sMLE estimated velocity uncertainty and the true value is smaller (0.41 vs 0.5 mm/year, only 1.2 times higher). Note that NNE estimates are much closer to the true value for all values of τ.

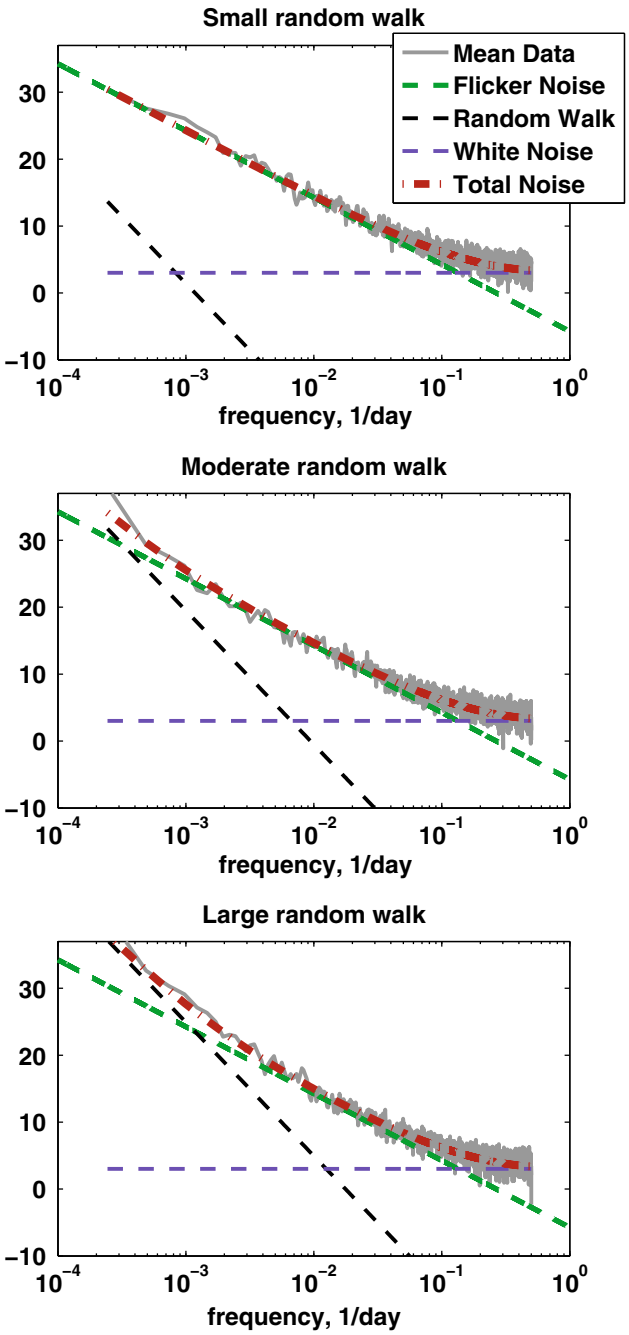

Fig. 5 Theoretical power spectral densities for different noise components (*dashed lines*) and empirical power spectrum densities (average of 20 spectra) for the data synthesized using the same parameters (*solid lines*). Amplitudes of flicker and white noise are held constant, while random walk is allowed to vary. Here, small random walk is $\tau = 0.1$ mm/year$^{0.5}$, moderate random walk is $\tau = 0.8$ mm/year$^{0.5}$, and large random walk is $\tau = 1.5$ mm/year$^{1.5}$

3.3 Anomalous random walk motion

NNE estimates a single random walk variance for the whole network of stations. Here, we explore the possibility that a single station with anomalously high random walk biases the network estimate, using synthetic data. Specifically, we create a network where one station has random walk of 3 mm/year$^{0.5}$ and nine stations have random walk of 0.3 mm/year$^{0.5}$. NNE estimates random walk at 1.22 mm/year$^{0.5}$ for this network, between the high and low values. As

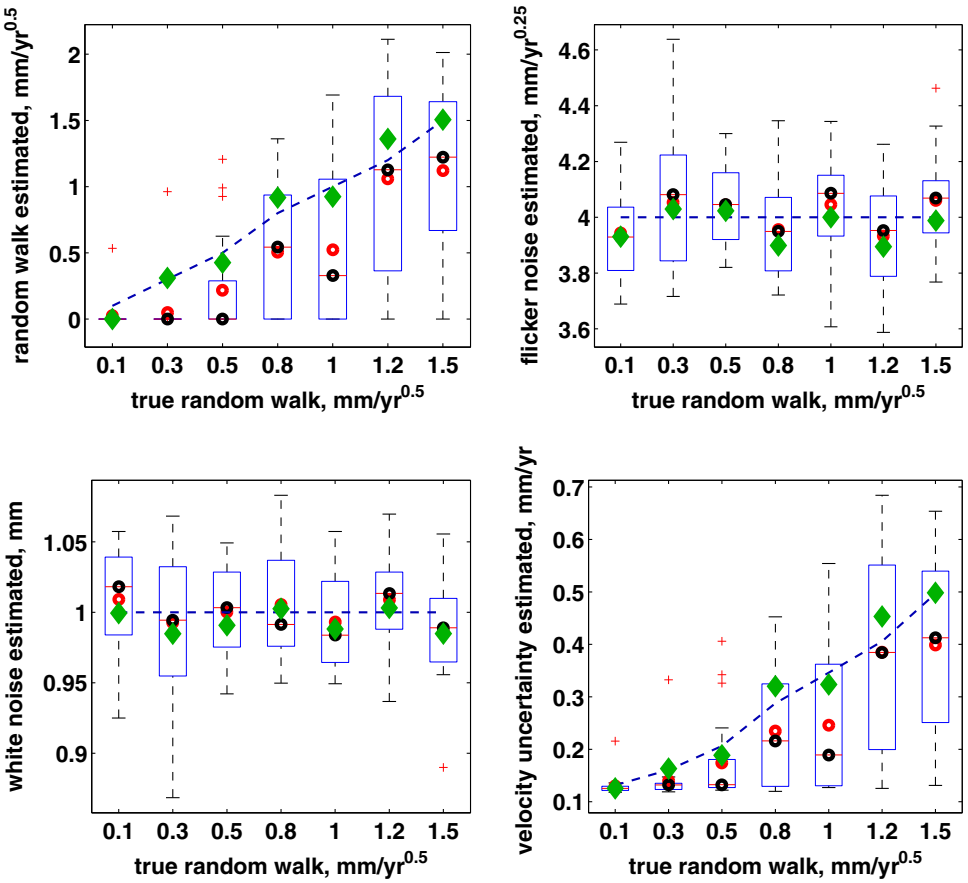

Fig. 6 Estimates of noise components from NNE and sMLE compared to true values (synthetic data). *Box plots* show the distribution of sMLE noise estimates for 20 time series for each set of noise parameters. *Red central mark with a black circle* indicates the median, *box edges mark* the 25th and 75th percentiles, and *whiskers* include the most extreme data, but exclude outliers shown by *red stars*. The average sMLE estimate is shown with a *red circle*. *Green diamonds* show NNE estimates of the parameters. *Blue dashed lines* indicate true values

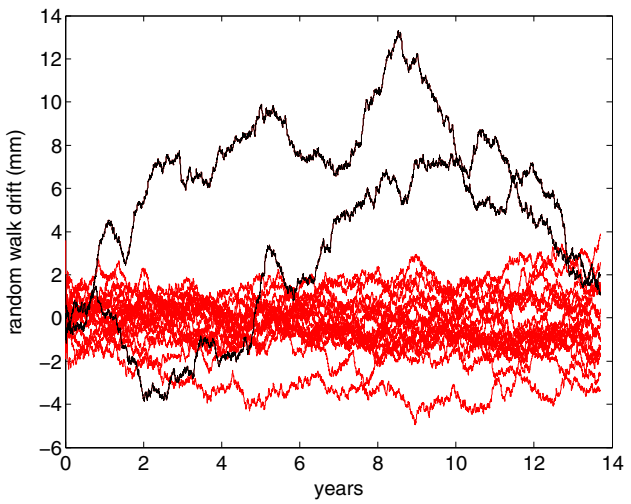

Fig. 7 Kalman filter output of random walk components for synthetic time series. 18 times series have random walk with $\tau = 0.3$ mm/year$^{0.5}$ (*red*), while 2 time series have random with $\tau = 3.0$ mm/year$^{0.5}$ (*black*). The anomalous time series are easily identified

expected with least-squares based estimators, the anomalously high value pulls the network estimate up.

We should be able to mitigate against this effect to some degree by examining the estimated random walk time series for the various stations. The NNE provides not only maximum likelihood estimates of the noise parameters, but also estimates of the different noise components for each station. Figure 7 illustrates the random walk components for each time series when the Kalman filter is run with the MLE estimates of the noise parameters. The east and north components of the anomalous station are clearly identifiable in this plot. The implication is that if the network estimate is contaminated by a few outlier stations, it should be easy to identify and remove the offending data.

4 Application to data from central and eastern USA

In this section, we apply the NNE to GPS time series from the central and eastern USA. The network is small (15 stations) and heterogeneous in terms of station quality. Thus, the derived network noise estimates are not representative of high-quality geodetic stations. Future work will incorporate more stations and subdivide them in terms of monument and other characteristics. However, application of the NNE to actual data and, in particular, comparison with standard MLE approaches is informative.

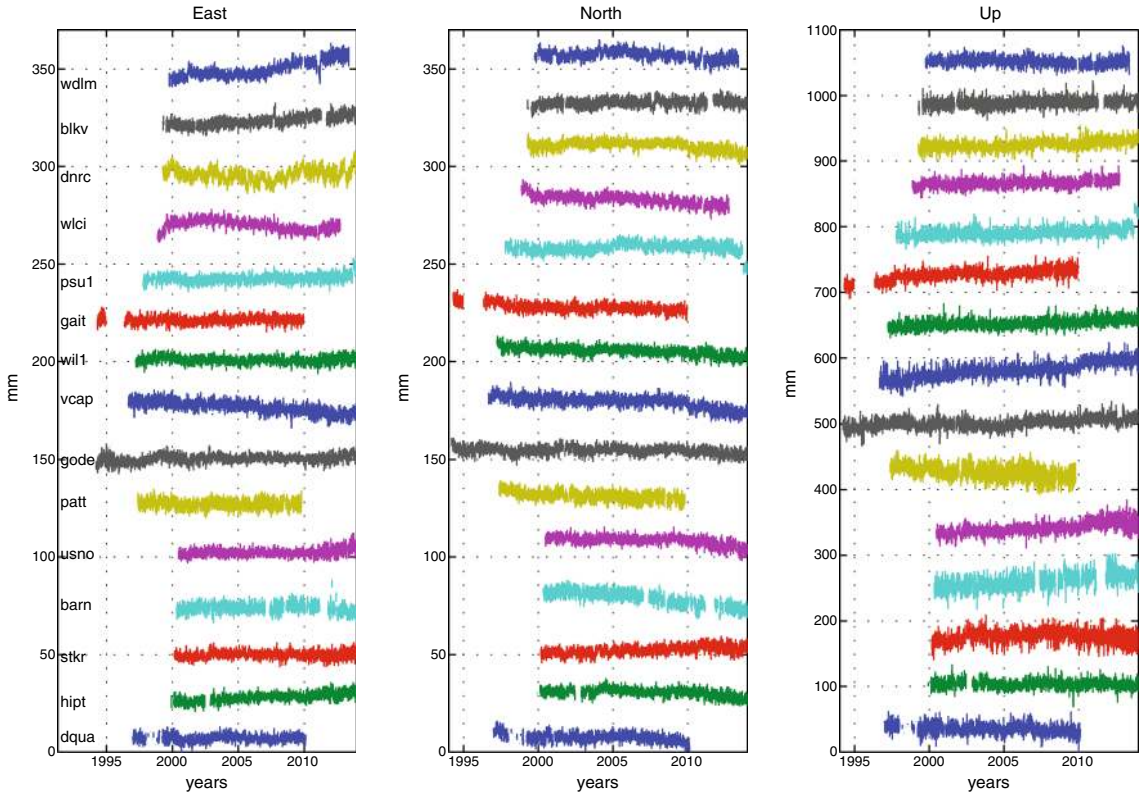

Fig. 8 *East*, *north* and *up* components of daily GPS position time series used in this paper. Station names are on the *left*. Arbitrary offsets for clarity. Note that the *y*-axis scale is different for *horizontal* and *vertical* components

4.1 Data

All the GPS data used in the study were processed with release 6.1 of the GIPSY software from the Jet Propulsion Laboratory. Non-fiducial daily GPS station coordinates were estimated using a precise point-positioning strategy (Zumberge et al. 1997). Constraints on the daily GPS solutions include a priori tropospheric hydrostatic and wet delays from Vienna Mapping Function (VMF1) parameters (http://ggosatm.hg.tuwien.ac.at), elevation- and azimuthally-dependent GPS and satellite antenna phase center corrections from IGS08 ANTEX files (available via ftp from ftp://sideshow.jpl.nasa.gov), and the FES2004 corrections for ocean tidal loading, which are in a Earth center-of-mass frame of reference (http://holt.oso.chalmers.se). GIPSY's single-station ambiguity resolution feature was used to resolve phase ambiguities (Bertiger et al. 2010). All daily station locations are expressed in IGS08, which conforms with ITRF2008 (Altamimi et al. 2011). The day-to-day scatter of the 3D continuous site locations with respect to station locations averaged over 30-day-long windows for each site averaged 2 mm (1σ) in the horizontal components and 4–6 mm in the vertical components prior to any correction for common-mode errors. The day-to-day scatter was reduced to 1 and 3 mm in the horizontal and vertical components, respectively, after correcting station coordinates for spatially coherent, common-mode noise following Márquez-Azúa and DeMets (2003).

The positions are rotated into the North American reference frame from ITRF2008. The Euler pole used for the transformation is located at 7.6 S, 88.3 W, with a rotation rate of 0.184°/Ma (Merkouriev and DeMets 2014). We chose 15 stations with the longest time series (spanning between 10 and 20 years; the average length is 14 years) and few data gaps. Outliers greater than 6 mm were removed using a median filter with a window of 20 days. Seasonal signals were removed with a notch filter with central period/bandwidth of 1/0.25 years, which removes the annual as well as the draconic period. It would be straightforward to add annual and semi-annual terms to the state-space model, however the notch filter does a better job of removing non-harmonic seasonal signals. We do not estimate a rotation pole, as rigid plate motion is already subtracted from the data. (This is equivalent to tightly constraining the pole in Eq. 1.)

We interpolate the predicted displacement due to GIA from the Stable North American Reference Frame (SNARF) model (Blewitt et al. 2005; Hill et al. 2010) onto the station locations using 2D cubic spline interpolation (Fig. 9), and then subtract it from the time series. The time series after the corrections described above are plotted in Fig. 8. We first

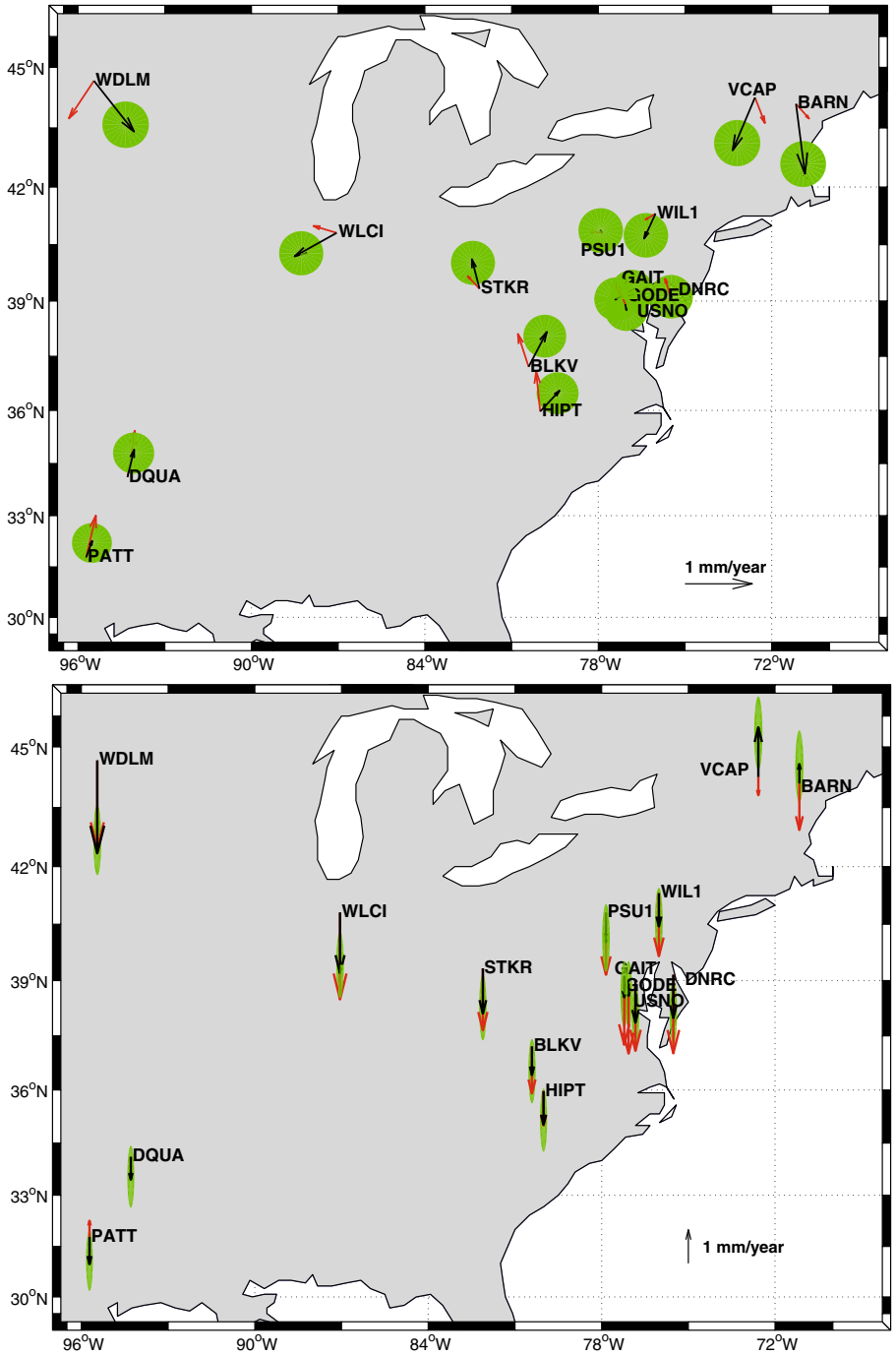

Fig. 9 GPS stations used in the preliminary estimation with velocities (prior to removal of common-mode errors) in fixed North American reference frame (*black vectors*). The *top panel* shows *horizontal* velocities, and the *bottom panel* shows *vertical*. The interpolated GIA velocities (from SNARF model) are in *red*, and the error *ellipses* (95 % confidence) for velocities calculated from the estimated noise parameters (for 15 years of data) are shown in *green*

analyze the cleaned time series as described above and next analyze those with common-mode errors removed following the approach of Márquez-Azúa and DeMets (2003).

The stations have various monument types, purposes, and quality. Six of the sites are maintained by state transportation departments (VCAP, WIL1, PSU1, DNRC, HIPT and STKR), six are maintained by NOAA/ESRL (WLCI, BLKV, WDLM, DQUA, BARN and PATT), two by NGS (GAIT and USNO), and one by NASA (GODE). The most common type of the monumentation is a steel mast on the top of a building (VCAP, WIL1, GAIT, PSU1, DNRC, HIPT and STKR), four stations are located on an antenna on the corner of a chain link fence (WLCI, WDLM, DQUA and PATT), two stations are monumented on concrete pillars with concrete bases (GODE and BLKV), one station is installed on a steel mast in concrete base (BARN) and one antenna is installed on a rod in a mortar rooftop parapet (USNO). Examples are shown in Fig. 12.

First, we analyzed the horizontal time series. We ran NNE on the north and east components simultaneously. With NNE,

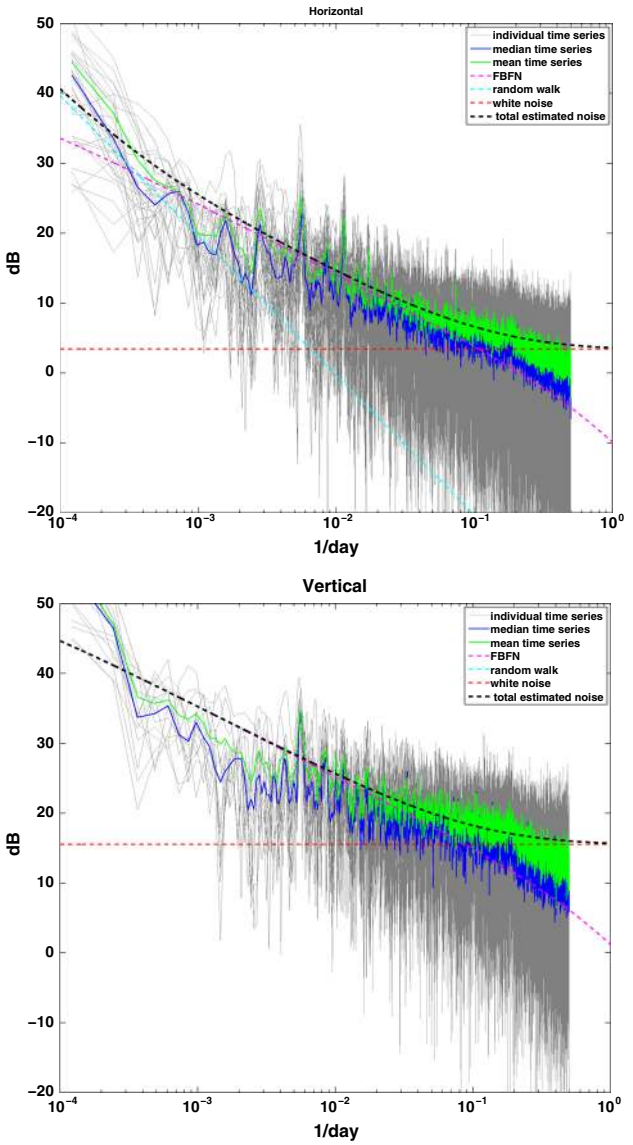

Fig. 10 Power spectrum of the individual times series is shown in *gray*, median power spectrum in *blue*, and average power spectrum in *green*. NNE estimated noise components and their sum are shown with *dashed lines*. The *top panel* shows the *horizontal* spectrum, and the *bottom panel* shows the *vertical*

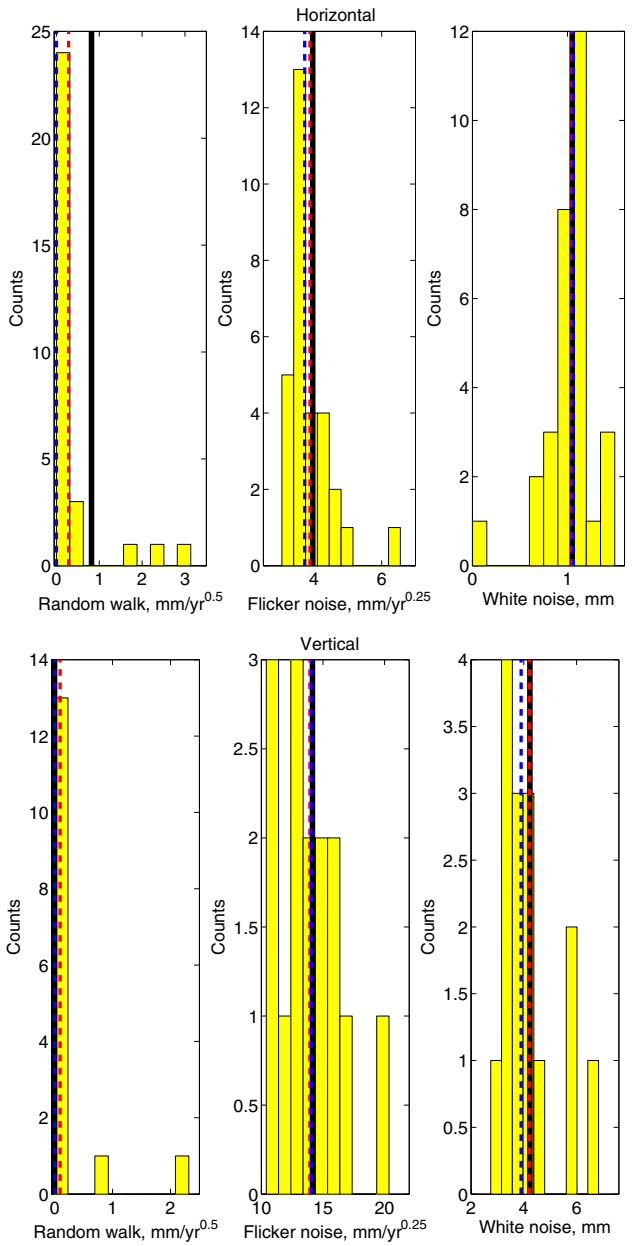

Fig. 11 NNE and sMLE noise estimates of *horizontal* (*top*) and *vertical* (*bottom*) time series. *Yellow histograms* show the distribution of noise parameters as estimated by sMLE. The mean sMLE noise parameter estimate is shown with a *red dashed line* and median with a *blue dashed line*. NNE estimates are shown with *black solid lines*

we found random walk $\tau = 0.82$ mm/year$^{0.5}$, flicker noise $\rho = 3.96$ mm/year$^{0.25}$, and white noise $\sigma = 1.05$ mm. The theoretical spectrum agrees well with the averaged spectrum for ten stations (20 components) as shown in Fig. 10. Note that the flicker noise fits the spectrum reasonably well at periods from approximately 10–1000 days. NNE and sMLE results are compared in Fig. 11. The NNE results for white and flicker noise are generally in agreement with the median of the sMLE results; however, our estimate for random walk is substantially higher. The median of the sMLE random walk estimates is zero, while the mean is 0.29 mm/year$^{0.5}$. Using the NNE estimates, the predicted velocity uncertainty is 0.29 mm/year with 10 years of data and 0.23 mm/year for 15 years of data. For the median sMLE estimates the predicted velocity uncertainties are two to three times lower: 0.12 mm/year for 10 years of data and 0.08 mm/year for 15 years.

We also analyzed the vertical time series. NNE finds no random walk, flicker noise $\rho = 7.92$ mm/year$^{0.25}$, and white noise $\sigma = 2.34$ mm. These estimates lead to predicted velocity uncertainties of 0.45 mm/year with 10 years of data. sMLE estimates are in good agreement with NNE for the vertical data.

4.2 Common-mode errors

There is considerable evidence that flicker and white noise are spatially correlated (Amiri-Simkooei 2009). Removing common-mode error decreases flicker noise in time series (Williams et al. 2004; Langbein 2012). We run NNE on the data, but with common mode removed based on the approach of Márquez-Azúa and DeMets (2003). The most significant change in the estimated parameters is in the flicker noise. For the horizontal time series, the flicker noise decreased from 3.96 to 2.55 mm/year$^{0.25}$ after the removal of common-mode errors. The vertical flicker noise decreased from 14.15 to 7.91 mm/year$^{0.25}$ after common-mode error removal. The white noise did not change significantly and the random walk estimate was slightly higher for the common-mode corrected data in the horizontal (0.95 vs 0.82 mm/year$^{0.5}$ originally) and significantly higher for the common-mode corrected vertical (2.21 vs 0 mm/year$^{0.5}$).

This indicates that the random walk and flicker noise estimates are negatively correlated, as expected.

5 Observations and discussion

Current estimates of flicker noise in GPS data differ substantially from study to study. Among the studies that used at least 7 years of data, the results vary from 2.6 to 7.5 mm/year$^{0.25}$ (Baldi et al. 2009; Santamaría-Gómez et al. 2012). The NNE estimate of flicker noise of 4 mm/year$^{0.25}$ for the data before removal of common-mode errors is well within that range. The common-mode corrected estimate of flicker noise, 2.55 mm/year$^{0.25}$, is on the lower side of the commonly cited results.

Contrary to some previous studies (e.g., Williams et al. 2004; Santamaría-Gómez et al. 2011; Amiri-Simkooei 2013; King and Williams 2009), we find non-negligible random walk. This could have several explanations. First, as shown in the synthetic tests above, our method of combining all the stations together for MLE is more sensitive to low values of random walk in the presence of flicker noise. Second, we analyzed much longer time series than previous studies, which makes it easier to detect random walk. Third, we analyzed data taken from antennas mounted on variable quality monuments (Fig. 12), so it is possible that a few stations with higher levels of random walk bias the estimate toward a higher value, since we estimate a single random walk variance for the whole network of stations.

NNE finds white and flicker noise in vertical time series significantly higher than in the horizontal, consistent with previously published results (Williams et al. 2004). However, NNE does not find any random walk in the vertical time series prior to removing common-mode errors. After removing the common-mode error, the random walk variance actually increases, which is likely due to trade-off with flicker noise, which decreased with removal of common-mode errors.

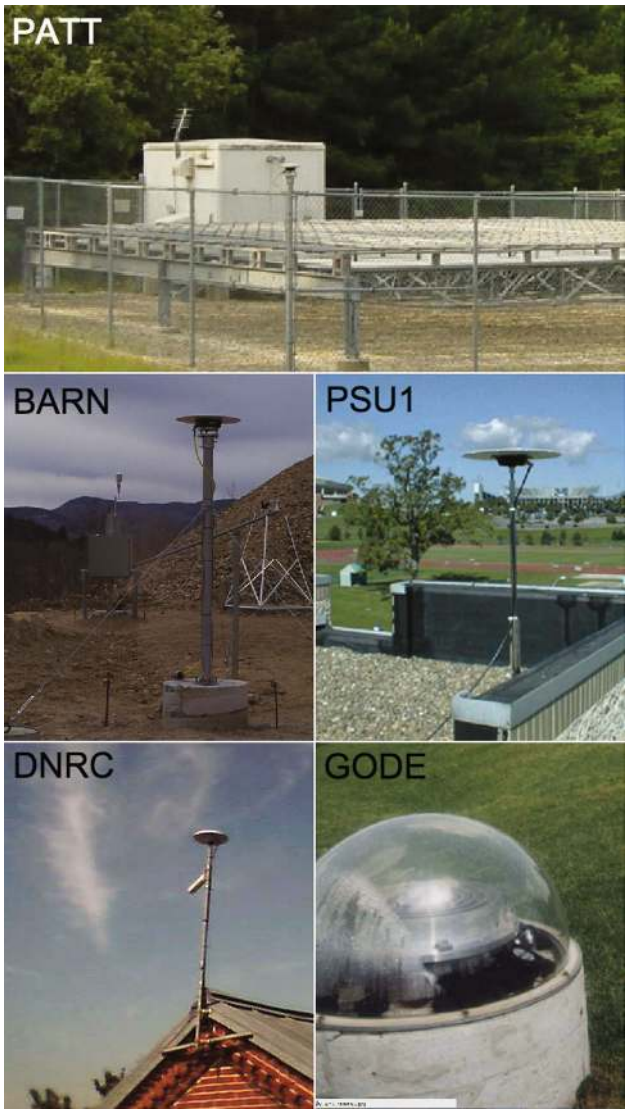

Fig. 12 Examples of station monuments (http://geodesy.noaa.gov/CORS/, http://www.profiler.noaa.gov/npn/). PATT is located on the corner of a chain link fence. DNRC and PSU1 are installed on metal masts on top of buildings. BARN's antenna is located on a metal mast in a concrete base. GODE is installed on a concrete pillar drilled into the ground

The estimated noise parameters, including that for flicker noise, differ depending on whether common-mode signals are removed or not. This is consistent with previous findings indicating that GPS noise is spatially correlated (Amiri-Simkooei 2009; Williams et al. 2004). In future implementations of the NNE, we could directly include spatial correlations in the state-space model, through the process of noise covariance.

In this study, we subtracted the predicted velocities due to plate rotation and GIA, without accounting for the uncer-

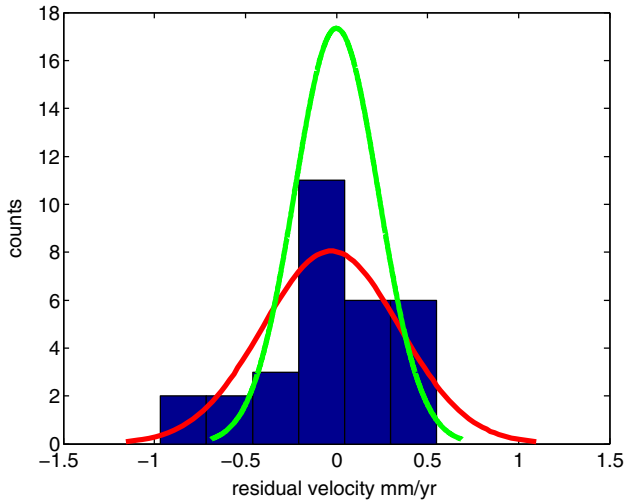

Fig. 13 Distribution of residual velocities is shown in the *histogram*. The *red curve* is the normal density function fitted to the *histogram*. The *green curve* is a normal distribution with zero mean and standard deviation equal to the velocity uncertainty of 0.23 mm/year for 15 years of data as estimated by the NNE

tainties in those values. As discussed in the method section, it is straightforward to include these processes directly in the state-space model. One might reasonably expect that uncertainties in plate rotation and GIA would influence the estimated noise parameters.

One could, for example, test an ensemble of GIA predictions and weight the resulting estimates by their respective likelihoods. However, we empirically observe the noise estimates are the same, whether or not the GIA velocities are removed from the time series. That is, a null GIA prediction does not change the results. More generally, we observe that subtracting (or adding) linear trends in the order of mm/year or less to the data does not affect the estimated noise parameters for daily sampled data. This is consistent with experience with sMLE where removing modest trends does not alter the noise estimates.

The main advantage of the NNE comes from maximizing the likelihood of the fit to the full network. As we have seen from the simulations, the mean of the individual time series maximum likelihood estimates is not equivalent to the network maximum likelihood estimate. While it is possible to compute the likelihood for a network without the Kalman filter, the Kalman filter-based network approach offers other advantages in that inclusion of spatial correlation should be straightforward and more general seasonal models can be implemented (Murray and Segall 2005). There is not a significant difference in computation time between NNE and a well-designed sMLE algorithm that factors the data covariance matrix; both are substantially faster than inverting the covariance directly.

Even with larger random walk than commonly reported, we find that the predicted velocity uncertainty is systematically smaller than the residual velocities with respect to North America (Fig. 13). According to our assumptions, after removing GIA and plate motion signals from the data, the residual time series should be composed solely of noise. With velocity uncertainty estimated at 0.23 mm/year for 15 years of data, we expect 95 % of the residual velocities to be less than 0.56 mm/year. However, we see in Fig. 13 that the distribution of residual velocities is wider than predicted from the theoretical velocity uncertainty. This suggests that the noise model is not capturing the true uncertainty in the data.

As discussed regarding GIA signals, modest, unmodeled trends barely influence the estimated random walk variance. Therefore, trends due to local processes may not be captured by the formal velocity uncertainty.

Other possible sources of error are undetected offsets. Williams (2003b) showed that the presence of such offsets can produce an error very similar to random walk. While the larger antenna offsets were removed from the data, it has been shown that there is no foolproof method for removing small offsets (Gazeaux et al. 2013), and these could certainly bias station velocities.

In this study, we estimated a single set of noise parameters characterizing a network of mixed quality sites (Fig. 12). However, we suspect that stations with poor monuments have larger random walk displacements than well-monumented stations, as a monument wobble is known to follow a random walk process (Wyatt 1989; Johnson and Agnew 1995). The relationship between random walk and monument types and materials has been explored previously (Williams et al. 2004; Langbein 2008; King and Williams 2009). In the future, we plan to subdivide stations into groups based on their monument and soil type, and estimate separate noise parameters for each group of stations. This will help us understand noise and velocity uncertainty for different types of monuments in different surface conditions.

6 Conclusions

We have introduced a NNE, which allows one to estimate random walk, flicker noise, and white noise variances for networks of continuous GPS stations. The NNE approach includes linear trends due to plate rotation, GIA, and potentially other well-characterized processes. Although not explicitly considered here, it is possible to include other noise types, as long as the the noise can be represented in a state-space model.

Based on synthetic tests, NNE provides accurate estimates of random walk variance, even with weak random walk. We therefore view NNE as a significant improvement over standard MLE approaches, in determining *representative* values

of noise parameters. While network estimates are intrinsically averages, we suggest that NNE is beneficial in accurately estimating random walk for groups of stations with with similar monument quality and soil type.

Preliminary NNE results with a small, very heterogeneous network of horizontal GPS time series from the central and eastern USA show larger random walk than estimated by standard MLE. Since even low values of random walk can greatly affect velocity uncertainty, previous estimates of velocity uncertainty may be optimistic. For example with 10 years of data, standard estimates yield 1σ uncertainties of 0.12 mm/year, whereas the network estimates are 0.29 mm/year, 2.4 times higher than traditional estimates.

We suggest that NNE can be used to develop representative error models for continuous GPS sites. This will lead to improved uncertainties in derived station velocities.

Appendix

Design matrices for first-order Gauss–Markov process

Here, we provide the state-space matrices for FBFN (Davis et al. 2005). The state transition matrix for the Gauss–Markov processes representing flicker noise is defined by:

$$\mathbf{F}_k^{\mathrm{FN}} = \begin{pmatrix} \exp(-\bar{f}_1 \delta t) & \dots & 0 \\ \vdots & \ddots & \vdots \\ 0 & \dots & \exp(-\bar{f}_m \delta t) \end{pmatrix}, \tag{14}$$

where m is the number of FOGM processes, $1/\bar{f}_m$ are time constants of the FOGM processes that are chosen to increase geometrically, and the spectral densities β_m are chosen such that all $\beta_m^2/2\bar{f}_m$ are equal. The covariance matrix is

$$\mathbf{Q}_k^{\mathrm{FN}} = \begin{pmatrix} \frac{1-\exp(-\bar{f}_1 \delta t)\beta_1}{2\bar{f}_1} & \dots & 0 \\ \vdots & \ddots & \vdots \\ 0 & \dots & \frac{1-\exp(-\bar{f}_m \delta t)\beta_m}{2\bar{f}_m} \end{pmatrix}. \tag{15}$$

Kalman filter formulation

Here, we provide the main Kalman filter equations (Welch and Bishop 1995). The recursive linear Kalman filter estimates the state vector x_k at each state t_k. The conditional mean $\hat{x}_{k|j}$ and covariance matrix $\Sigma_{k|j}$ at epoch k given data through epoch j are

$$\hat{x}_{k|j} = E\left[x_k \mid d_1, \dots, d_j\right], \tag{16}$$
$$\Sigma_{k|j} = \mathrm{Cov}\left[x_k \mid d_1, \dots, d_j\right]. \tag{17}$$

The left side of (16) is read "$\hat{x}$ at k given j".

The conditional means and covariances satisfy the one-step-ahead prediction equations,

$$\hat{x}_{k+1|k} = F_{k+1}\, \hat{x}_{k|k} \tag{18}$$
$$\Sigma_{k+1|k} = F_{k+1}\, \Sigma_{k|k}\, F_{k+1}^T + Q_{k+1}, \tag{19}$$

and the update equations

$$\hat{x}_{k|k} = \hat{x}_{k|k-1} + G_k v_k \tag{20}$$
$$\Sigma_{k|k} = \Sigma_{k|k-1} - G_k\, H_k\, \Sigma_{k|k-1}, \tag{21}$$

where v_k is the innovation. The innovation, or the prediction residual, is the difference between the observed data at time t_k and the predicted data. The predicted data are calculated using the state vector given data up to time t_{k-1}

$$v_k \equiv d_k - H_k\, \hat{x}_{k|k-1}, \tag{22}$$

and the Kalman gain G_k is given by

$$G_k \equiv \Sigma_{k|k-1}\, H_k^T \left(R_k + H_k\, \Sigma_{k|k-1}\, H_k^T\right)^{-1}. \tag{23}$$

The Kalman filter starts with a prior estimate $\hat{x}_{1|0}$ and covariance $\Sigma_{1|0}$. The prior may be precise, reflecting a priori information from previous studies, or may have a large uncertainty. The first observation d_1 is used to update the state (20) and (21), which leads to the posterior mean $\hat{x}_{1|1}$ and associated covariance $\Sigma_{1|1}$. Following this, $\hat{x}_{2|1}$ and its covariance are estimated using the prediction Eqs. (18) and (19), and so on.

Acknowledgments We thank James Davis (Columbia University) for providing the SNARF GIA model. We acknowledge Sang-Ho Yun for writing the notch filter code. We appreciate fruitful discussions and computational help from Andrew Bradley. We thank the reviewer Matt King, editor Simon Williams, and two anonymous reviewers for extremely helpful suggestions. This work was supported by NASA Headquarters under the NASA Earth and Space Science Fellowship Program—Grant 14-EARTH14R-47 and by the USGS Grant G13AP00020.

References

Agnew D (1992) The time-domain behavior of power-law noises. Geophys Res Lett 19(4):333–336. doi:10.1029/91GL02832

Altamimi Z, Collilieux X, Métivier L (2011) ITRF2008: an improved solution of the international terrestrial reference frame. J Geod 85(8):457–473. doi:10.1007/s00190-011-0444-4

Amiri-Simkooei A (2009) Noise in multivariate GPS position time-series. J Geod 83(2):175–187. doi:10.1007/s00190-008-0251-8

Amiri-Simkooei A (2013) On the nature of GPS draconitic year periodic pattern in multivariate position time series. J Geophys Res Solid Earth 118(5):2500–2511

Amiri-Simkooei A, Tiberius C, Teunissen P (2007) Assessment of noise in GPS coordinate time series: methodology and results. J Geophys Res 112(B7). doi:10.1029/2006jb004913

Baldi P, Casula G, Cenni N, Loddo F, Pesci A (2009) GPS-based monitoring of land subsidence in the Po Plain (Northern Italy). Earth Planet Sci Lett 288:204–212. doi:10.1016/j.epsl.2009.09.023

Bennett R, Wernicke B, Niemi N, Friedrich A, Davis J (2003) Contemporary strain rates in the northern Basin and Range province from GPS data. Tectonics 22(2). doi:10.1029/2001tc001355

Bertiger W, Desai SD, Haines B, Harvey N, Moore AW, Owen S, Weiss JP (2010) Single receiver phase ambiguity resolution with GPS data. J Geod 84(5):327–337. doi:10.1007/s00190-010-0371-9

Blewitt G et al (2005) A Stable North American Reference Frame (SNARF): first release. In: The SNARF Working Group, UNAVCO, Stevenson

Bonforte A, Puglisi G (2006) Dynamics of the eastern flank of Mt. Etna volcano (Italy) investigated by a dense GPS network. J Volcanol Geotherm Res 153(3):357–369. doi:10.1016/j.jvolgeores.2005.12.005

Calais E, Stein S (2009) Time-variable deformation in the new Madrid seismic zone. Science 323(5920):1442–1442. doi:10.1126/science.1168122

Calais E, Han J, DeMets C, Nocquet J et al (2006) Deformation of the North American plate interior from a decade of continuous GPS measurements. J Geophys Res 111(B06):402. doi:10.1029/2005jb004253

Davis J, Greenhall C, Stacey P (2005) A Kalman filter clock algorithm for use in the presence of flicker frequency modulation noise. Metrologia 42:1. doi:10.1088/0026-1394/42/1/001

Frankel A, Smalley R, Paul J (2012) Significant motions between GPS sites in the New Madrid Region: implications for seismic hazard. Bull Seismol Soc Am 102(2):479–489. doi:10.1785/0120100219

Gazeaux J, Williams S, King M, Bos M, Dach R, Deo M, Moore AW, Ostini L, Petrie E, Roggero M et al (2013) Detecting offsets in GPS time series: first results from the detection of offsets in GPS experiment. J Geophys Res Solid Earth 118(5):2397–2407. doi:10.1002/jgrb.50152

Hackl M, Malservisi R, Hugentobler U, Wonnacott R (2011) Estimation of velocity uncertainties from GPS time series: examples from the analysis of the South African TrigNet network. J Geophys Res 116(B11):B11404. doi:10.1029/2010jb008142

Hill EM, Davis JL, Tamisiea ME, Lidberg M (2010) Combination of geodetic observations and models for glacial isostatic adjustment fields in Fennoscandia. J Geophys Res 115(B7). doi:10.1029/2009jb006967

Jiang W, Deng L, Li Z, Zhou X, Liu H (2014) Effects on noise properties of GPS time series caused by higher-order ionospheric corrections. Adv Space Res 53(7):1035–1046. doi:10.1016/j.asr.2013.12.037

Johnson H, Agnew D (1995) Monument motion and measurements of crustal velocities. Geophys Res Lett 22(21):2905–2908. doi:10.1029/95gl02661

King MA, Watson CS (2010) Long GPS coordinate time series: multipath and geometry effects. J Geophys Res 115(B4). doi:10.1029/2009jb006543

King MA, Williams S (2009) Apparent stability of GPS monumentation from short-baseline time series. J Geophys Res 114(B10). doi:10.1029/2009jb006319

King MA, Altamimi Z, Boehm J, Bos M, Dach R, Elosegui P, Fund F, Hernández-Pajares M, Lavallee D, Cerveira PJM et al (2010) Improved constraints on models of glacial isostatic adjustment: a review of the contribution of ground-based geodetic observations. Surv Geophys 31(5):465–507. doi:10.1007/s10712-010-9100-4

Kirchner JW (2005) Aliasing in 1/f α noise spectra: origins, consequences, and remedies. Phys Rev E 71(6). doi:10.1103/physreve.71.066110

Kusche J, Schrama E (2005) Surface mass redistribution inversion from global GPS deformation and Gravity Recovery and Climate Experiment (GRACE) gravity data. J Geophys Res 110(B9). doi:10.1029/2004jb003556

Langbein J (2004) Noise in two-color electronic distance meter measurements revisited. J Geophys Res 109(B04):406. doi:10.1029/2003jb002819

Langbein J (2008) Noise in GPS displacement measurements from Southern California and Southern Nevada. J Geophys Res 113(B05):405. doi:10.1029/2007jb005247

Langbein J (2012) Estimating rate uncertainty with maximum likelihood: differences between power-law and flicker-random-walk models. J Geod 86(9):775–783. doi:10.1007/s00190-012-0556-5

Langbein J, Johnson H (1997) Correlated errors in geodetic time series: implications for time-dependent deformation. J Geophys Res 102(B1):591–603. doi:10.1029/96jb02945

Lidberg M, Johansson JM, Scherneck HG, Davis JL (2007) An improved and extended GPS-derived 3D velocity field of the glacial isostatic adjustment (GIA) in Fennoscandia. J Geod 81(3):213–230. doi:10.1007/s00190-006-0102-4

Liu M, Yang Y, Stein S, Zhu Y, Engeln J (2000) Crustal shortening in the Andes: why do GPS rates differ from geological rates? Geophys Res Lett 27(18):3005–3008. doi:10.1029/2000gl008532

Lü WC, Cheng SG, Yang HS, Liu DP (2008) Application of GPS technology to build a mine-subsidence observation station. J China Univ Min Technol 18(3):377–380. doi:10.1016/s1006-1266(08)60079-6

Mao A, Harrison C, Dixon T (1999) Noise in GPS coordinate time series. J Geophys Res 104(B2):2797–2816. doi:10.1029/1998jb900033

Márquez-Azúa B, DeMets C (2003) Crustal velocity field of Mexico from continuous GPS measurements, 1993 to June 2001: implications for the neotectonics of Mexico. J Geophys Res 108(B9). doi:10.1029/2002jb002241

Merkouriev S, DeMets C (2014) High-resolution estimates of Nubia–North America plate motion: 20 Ma to present. Geophys J Int 196(3):1281–1298. doi:10.1093/gji/ggt463

Murray J, Segall P (2005) Spatiotemporal evolution of a transient slip event on the San Andreas fault near Parkfield, California. J Geophys Res 110(B9). doi:10.1029/2005jb003651

Papanikolaou ID, Roberts GP, Michetti AM (2005) Fault scarps and deformation rates in Lazio-Abruzzo, Central Italy: comparison between geological fault slip-rate and GPS data. Tectonophysics 408(1):147–176. doi:10.1016/j.tecto.2005.05.043

Pritchard M, Simons M, Rosen P, Hensley S, Webb F (2002) Co-seismic slip from the 1995 July 30 Mw = 8.1 Antofagasta, Chile, earthquake as constrained by InSAR and GPS observations. Geophys J Int 150(2):362–376. doi:10.1046/j.1365-246x.2002.01661.x

Psimoulis P, Ghilardi M, Fouache E, Stiros S (2007) Subsidence and evolution of the Thessaloniki plain, Greece, based on historical leveling and GPS data. Eng Geol 90(1):55–70. doi:10.1016/j.enggeo.2006.12.001

Puskas C, Smith R, Meertens C, Chang W (2007) Crustal deformation of the Yellowstone–Snake River Plain volcano-tectonic system: campaign and continuous GPS observations, 1987–2004. J Geophys Res 112(B3). doi:10.1029/2006jb004325

Ray J, Altamimi Z, Collilieux X, van Dam T (2008) Anomalous harmonics in the spectra of GPS position estimates. GPS Solut 12(1):55–64. doi:10.1007/s10291-007-0067-7

Santamaría-Gómez A, Bouin M, Collilieux X, Wöppelmann G (2011) Correlated errors in GPS position time series: implications for velocity estimates. J Geophys Res 116(B1):B01405. doi:10.1029/2010jb007701

Santamaría-Gómez A, Gravelle M, Collilieux X, Guichard M, Míguez BM, Tiphaneau P, Wöppelmann G (2012) Mitigating the effects of vertical land motion in tide gauge records using a state-of-the-art GPS velocity field. Glob Planet Chang 98:6–17. doi:10.1016/j.gloplacha.2012.07.007

Segall P, Davis JL (1997) GPS applications for geodynamics and earthquake studies. Ann Rev Earth Planet Sci 25(1):301–336. doi:10.1146/annurev.earth.25.1.301

Segall P, Matthews M (1997) Time dependent inversion of geodetic data. J Geophys Res 102(B10):22391. doi:10.1029/97jb01795

Serpelloni E, Anzidei M, Baldi P, Casula G, Galvani A (2005) Crustal velocity and strain-rate fields in Italy and surrounding regions: new results from the analysis of permanent and non-permanent

GPS networks. Geophys J Int 161(3):861–880. doi:10.1111/j.1365-246x.2005.02618.x

Teferle F, Bingley R, Williams S, Baker T, Dodson A (2006) Using continuous GPS and absolute gravity to separate vertical land movements and changes in sea-level at tide-gauges in the UK. Philos Trans R Soc A Math Phys Eng Sci 364(1841):917–930. doi:10.1098/rsta.2006.1746

Thatcher W (2003) GPS constraints on the kinematics of continental deformation. Int Geol Rev 45(3):191–212. doi:10.2747/0020-6814.45.3.191

Tremayne AR, Harvey AC (1983) Time series models. Economica 50(198):216. doi:10.2307/2554073

Welch O, Bishop G (1995) An introduction to the kalman filter. Technical Report 95-041, University of North Carolina at Chapel Hill

Williams S (2003a) The effect of coloured noise on the uncertainties of rates estimated from geodetic time series. J Geod 76(9):483–494. doi:10.1007/s00190-002-0283-4

Williams S (2003b) Offsets in Global Positioning System time series. J Geophys Res 108(B6). doi:10.1029/2002jb002156

Williams S, Bock Y, Fang P, Jamason P, Nikolaidis R, Prawirodirdjo L, Miller M, Johnson D (2004) Error analysis of continuous GPS position time series. J Geophys Res 109(B3):B03412. doi:10.1029/2003jb002741

Wöppelmann G, Martin Miguez B, Bouin MN, Altamimi Z (2007) Geocentric sea-level trend estimates from GPS analyses at relevant tide gauges world-wide. Glob Planet Chang 57(3):396–406. doi:10.1016/j.gloplacha.2007.02.002

Wyatt FK (1989) Displacement of surface monuments: vertical motion. J Geophys Res 94(B2):1655–1664. doi:10.1029/jb094ib02p01655

Zhang J, Bock Y, Johnson H, Fang P, Williams S, Genrich J, Wdowinski S, Behr J (1997) Southern california permanent GPS geodetic array: error analysis of daily position estimates and site velocities. J Geophys Res 102:18–18. doi:10.1029/97jb01380

Zumberge J, Heflin M, Jefferson D, Watkins M, Webb F (1997) Precise point positioning for the efficient and robust analysis of GPS data from large networks. J Geophys Res 102(B3):5005–5017. doi:10.1029/96jb03860